Post-Print of an Accepted Manuscript on the Laboratory of Turbulent Flows Website

Complete citation:

Gibeau, B., Koch, C. R., & Ghaemi, S. (2018). Secondary instabilities in the wake of an elongated two-dimensional body with a blunt trailing edge. *Journal of Fluid Mechanics*, *846*, 578-604. doi: 10.1017/jfm.2018.285

The final publication is available at https://doi.org/10.1017/jfm.2018.285

The Accepted Manuscript begins on the next page.

Secondary instabilities in the wake of an elongated two-dimensional body with a blunt trailing edge

B. Gibeau[1], C. R. Koch[1] and S. Ghaemi[1]†

[1]Department of Mechanical Engineering, University of Alberta, Edmonton, Alberta T6G 2R3, Canada

(Received xx; revised xx; accepted xx)

The secondary instability in the wake of a two-dimensional blunt body with a chord to thickness ratio of 46.5 was experimentally investigated for Reynolds numbers of 3500, 5200, and 7000 based on blunt trailing edge height h. Planar, stereoscopic, and high-speed particle image velocimetry (PIV) measurements were performed to characterise the wake and upstream boundary layer. The same mode B secondary instability that is found in the cylinder wake was found to be present in the wake of the elongated body studied here. The most probable wavelength of the secondary instability, defined as the spanwise distance between adjacent streamwise vortex pairs in the wake, was found to range from 0.7-0.8h by applying a spatial autocorrelation to spanwise-wall-normal instantaneous fields of Q-criterion. The temporal evolution of the secondary wake vortices was investigated using time-resolved stereoscopic PIV measurements and it was shown that the vortices maintain both their directions of rotation and spanwise positions during the primary vortex shedding cycles. In agreement with previous literature, the secondary instability did not greatly change as the upstream boundary layer transitioned from laminar to turbulent. Moreover, any upstream boundary layer structures were found to rapidly evolve into wake structures just past the blunt trailing edge. The wavelength of the secondary instability was shown to match the spanwise distance between adjacent low-speed zones of streamwise velocity in the wake. These undulating velocity patterns proved to be a viable method for determining the secondary instability wavelength; however, this type of analysis is highly sensitive to the energy content used for data reconstruction when proper orthogonal decomposition is applied beforehand.

Key words:

1. Introduction

Vortex shedding is a well-documented flow phenomenon that dominates the wakes of non-streamlined, two-dimensional bodies at Reynolds numbers (Re) above the Stokes regime. An unsteady interaction between separated shear layers at the trailing edge causes periodic shedding of vortices, leading to unwanted structural vibrations (Williamson & Govardhan 2004), acoustic noise (Brooks *et al.* 1989), and pressure drag (Roshko 1993). While many different body geometries have been used to study vortex shedding in the past, the circular cylinder has been the most popular by far (Williamson 1996*b*). This

† Email address for correspondence: ghaemi@ualberta.ca

work will focus on a simplified version of a geometry that has received less attention but remains important to engineering applications: the blunt trailing edge (BTE) airfoil. One example of this geometry is found on large wind turbine blades. Applying a BTE near the root of a wind turbine blade can significantly reduce its weight and improve the structural performance of the cross section (Jackson *et al.* 2005). Furthermore, numerical and experimental work has shown that blunting the trailing edge of an airfoil allows for pressure recovery in the wake region, resulting in improved lift characteristics and a reduction in sensitivity to premature boundary layer transition (Standish & van Dam 2003; Baker *et al.* 2006). These benefits extend to the wings of large aircraft; however, in both applications, the benefits are accompanied by the previously mentioned undesired effects. An improved understanding of unsteady wake dynamics could lead to developing wake suppression techniques that allow for the utilization of blunted airfoils without negative side effects.

Vortex shedding begins when a shear layer instability leads to skewed vorticity in the wake (Zdravkovich 1969). This is accompanied by a pressure gradient that drives the initial rolling-up process. The affected shear layer forms into a vortex which grows in strength until it pulls the opposing shear layer across the wake centre line, effectively cutting off the growth and forcing the vortex to detach from the body (Gerrard 1966). At this point, the vorticity concentration in the wake is once again asymmetric and the cycle repeats. This process forms the well-known von Kármán vortex street and has been shown to begin as low as $Re(d) = 40$ in the case of a circular cylinder with diameter d (Roshko 1954) and $Re(h) = 154$ in the case of a two-dimensional body with a BTE of height h (Petrusma & Gai 1996). Further increasing Re leads to the onset of three-dimensionality in the wake and eventually a transition to turbulence, which occurs by either large-scale distortion of the primary spanwise vortices or by the amplification of Tollmien-Schlichting waves in the separated shear layers (Bloor 1964). The large-scale distortions are a result of abnormalities within the wake region, usually in the form of oblique vortex shedding (Williamson 1989) or vortex dislocations (Williamson 1992). The latter can exist when adjacent segments of the wake experience different shedding frequencies. This is referred to as cellular vortex shedding and has been shown to exist in different forms (Scarano & Poelma 2009).

This paper is concerned with counter-rotating streamwise vortex pairs that are found within the three-dimensional wake. As opposed to the primary shedding of large spanwise vortices, the much smaller streamwise vortex pairs represent the secondary wake instability and vary depending on body geometry and Re. In an early observation, Gerrard (1978) described them as "fingers of dye" during flow visualization experiments, although he did not associate them with a secondary instability at the time. Nearly a decade later, Wei & Smith (1986) detected streamwise vortices in the wake of a circular cylinder and concluded that they were a direct result of the Tollmien-Schlichting transition waves in the separated shear layer observed by Bloor (1964). Shortly after, Williamson (1988) showed the existence of two stages of three-dimensional transition in the unforced wake of a circular cylinder consisting of two unique instability modes: mode A and mode B. Contrary to the work of Wei & Smith (1986), Williamson (1988) concluded that the secondary vortices cannot be a result of the Tollmien-Schlichting transition waves because the vortices appear prior to their amplification.

The secondary instabilities in the unforced wake of a circular cylinder continued to be actively investigated during the 1990s (Bays-Muchmore & Ahmed 1993; Mansy *et al.* 1994; Wu *et al.* 1994; Lin *et al.* 1995; Zhang *et al.* 1995; Brede *et al.* 1996; Wu *et al.* 1996; Williamson 1996*a*). The generally agreed upon results are described next. Mode A is the first to appear and features vortex loops which form streamwise vortex pairs in

an out-of-phase arrangement. The spacing between adjacent vortex pairs, which will be referred to as the secondary instability wavelength, is approximately 3-5d, and a distinct characteristic of mode A is the fact that the vortex pairs change their sense of rotation every half shedding cycle of the primary instability. Mode B replaces mode A as Re is increased and consists of a much finer in-phase spatial arrangement of streamwise vortex pairs which have a secondary instability wavelength of approximately 1d. The mode B vortex pairs weave between the primary spanwise vortices, effectively maintaining their rotational orientation for many shedding cycles. Mode B dominates the unforced cylinder wake for all appreciable Re.

A third instability mode, mode S, has been predicted by stability analysis and has the potential to occur in the unforced wake of square cylinders in addition to modes A and B (Robichaux *et al.* 1999). Mode S contains in-phase vortex pairs with a secondary instability wavelength of 2.8h. These vortex pairs differ from those of modes A and B because their direction of rotation changes every shedding cycle of the primary instability. Robichaux *et al.* (1999) concluded that mode S is not the most unstable of the square cylinder modes and so modes A and B may need to be suppressed in order to show its existence. They also concluded that mode S is a subharmonic mode (hence its name), but this was shown to be incorrect, as it is actually quasi-periodic in nature (Blackburn & Lopez 2003). For this reason it is more appropriately referred to as mode QP (Blackburn *et al.* 2005). Finally, a fourth secondary instability mode has the potential to exist when the trailing edge geometry breaks the wake symmetry. This mode is referred to as mode C and may exist in cases such as flow past square cylinders with an angle of incidence (Sheard *et al.* 2009) or circular cylinders with trailing edge disturbances (Yildirim *et al.* 2013).

There is strong evidence that mode A is the result of an elliptical instability within the primary spanwise vortices (Thompson *et al.* 2001); however, the origin of the mode B instability is not clear from past literature. As previously mentioned, Wei & Smith (1986) attribute the vortices to Tollmien-Schlichting transition waves. Wu *et al.* (1994) emphasise that the stretching of initial vorticity tubes within the separated shear layers plays a major role in the development of the streamwise vortices. These initial vortex tubes may take the form of Kelvin-Helmholtz vortices that are embedded within the separated shear layers which form the primary spanwise vortices (Lin *et al.* 1995). Brede *et al.* (1996) have shown the existence of mode B as close as 0.2d downstream from the trailing edge and suggest that it is the result of a shear layer instability that arises due to fluid interacting with the cylinder. Williamson (1996*a*) suggests that mode B is due to an instability within the braid region between interacting shear layers, and the in-phase arrangement of mode B is due to the close proximity of braid shear layers. The recently formed streamwise vortices force the same spanwise location upon the newly forming vortex pairs. This "imprinting" process has more recently been demonstrated in the near-wake of a square cylinder (Luo *et al.* 2007), although it does not account for the inception of the first streamwise vortices. Overall, the instability that forms mode B is different than the one that forms mode A.

The BTE airfoil has been simplified in the literature as a flat plate with an elliptical leading edge and a BTE. This geometry will be referred to as an elongated blunt body from here forward. The secondary instabilities in the wake of the elongated blunt body have not been given much attention in the past. An early investigation by Ryan *et al.* (2005) utilised direct numerical simulations and Floquet stability analysis to probe the wakes of elongated blunt bodies with varying aspect ratios, where aspect ratio AR is defined as the ratio between chord length c and trailing edge height h. For $AR = 2.5$, 7.5, 12.5, and 17.5 and $Re(h)$ up to 700, a key result is that AR affects which modes

will appear in the wake. The circular cylinder mode A has the potential to be the most unstable for $AR < 7.5$; however, $AR > 7.5$ are susceptible to a new dominant mode. This new mode is similar to mode B of a circular cylinder in that it features streamwise vortex pairs which maintain their directions of rotation during primary shedding cycles, but it has a predicted secondary instability wavelength of $2.2h$ and also has differences in the near-wake vorticity field. For these reasons, the authors referred to it as mode B$'$. For large AR, a third instability mode was predicted to become more unstable than Mode A. This mode was referred to as mode S$'$ due to its similarities with the square cylinder mode S. It has a secondary instability wavelength of 0.7-1.0h and the streamwise vortex pairs change their direction of rotation after each full shedding cycle. Mode S$'$ seems to have more in common with the cylinder mode B than the BTE mode B$'$ because of their similar secondary instability wavelengths and near-wake vorticity fields. Mode S$'$ is the least unstable mode for $12.5 < AR < 17.5$ but more unstable than mode A for $AR > 17.5$. The prediction that the instability modes vary with AR suggests that the upstream boundary layer, which would be more developed for large AR, plays a role in the formation of the secondary instabilities. Additionally, the differences in the near-wake vorticity fields may be a result of the more developed upstream boundary layer that accompanies large AR.

It has been shown by Mansy *et al.* (1994) and Wu *et al.* (1996) that the secondary instability wavelength matches the spanwise distance between adjacent low-speed zones of streamwise velocity in the wake region. These undulating velocity patterns have been used to provide evidence for the existence of the mode B$'$ instability in the wake of an elongated blunt body with $AR = 12.5$ and $250 \leqslant Re(h) \leqslant 5 \times 10^4$ by Naghib-Lahouti *et al.* (2012, 2014). Both investigations found secondary instability wavelengths varying from 2.0 to 2.5h. Naghib-Lahouti *et al.* (2012) also observed that the vortex pairs maintained their sense of rotation based on visual inspection of laser induced fluorescence (LIF) images. They concluded that mode B$'$ was present for the geometry in question, and that the secondary instability has limited dependence on the state of the upstream boundary layer. To the authors knowledge, this is the only experimental evidence of mode B$'$ within past literature. Additionally, there does not appear to be any investigation into the wake organisation of elongated blunt bodies with large AR, and this has motivated the present study.

Considering the literature reviewed here, it is evident that the understanding of elongated blunt body wakes is limited despite the large amount of work done on the wakes of cylinders. Moreover, the effect that coherent boundary layer structures may have on the wake structures has not been extensively investigated in the past. This study focuses on increasing the understanding of these topics. The primary focus is twofold:

(i) Provide experimental insight regarding the wake modes of a highly elongated blunt body. The analysis will extend the numerical predictions made by Ryan *et al.* (2005) for $2.5 \leqslant AR \leqslant 17.5$ and also the experimental investigations of Naghib-Lahouti *et al.* (2012, 2014) at $AR = 12.5$ to a larger AR of 46.5, which is more relevant to industrial applications. Specifically, the secondary instability in the wake will be statistically characterised in terms of spanwise wavelength and the spatio-temporal symmetry of the vortices.

(ii) Investigate the effect that the upstream boundary layer state has on the secondary instability in the wake and characterise the boundary layer structures during transition past the BTE. The impact of a laminar, transitional, and turbulent upstream boundary layer will be studied.

The current investigation begins by characterising the state of boundary layer upstream from the BTE to ensure the selected Re cover the laminar, transitional, and turbulent

upstream cases of interest. The wavelength of the secondary instability is then statistically investigated by applying an autocorrelation technique to the vorticity field. The spatio-temporal symmetry of the wake is investigated both qualitatively and statistically using time-resolved measurements. Together, these analyses fully characterise the spatio-temporal behaviour of the secondary vortices. The relationship between the secondary instability and the upstream boundary layer is explored by tracking the spacing and evolution of the low-speed structures in the boundary layer as they move past the BTE and by determining the strength of the streamwise vortices in both the boundary layer and wake. Finally, the proper-orthogonal-decomposition-based analysis used by Naghib-Lahouti *et al.* (2012, 2014) is applied here to compare the present results with previous estimations of the secondary instability wavelength.

2. Experimental Setup

The boundary layer and wake flows near the BTE of an elongated blunt body model were measured using separate particle image velocimetry (PIV) configurations which included two planar (2C-PIV) and two stereoscopic (stereo-PIV) measurements in three orthogonal viewing planes. They were conducted in a closed-loop wind tunnel at freestream velocities of 2.3, 4.3, 6.3, 8.4, and 10.4 m s^{-1}, corresponding to $Re(h) = 1900$, 3500, 5200, 7000, and 8700 where h is the BTE height of the model.

2.1. *Wind Tunnel Facility and Elongated Blunt Body Model*

The test section of the wind tunnel is rectangular with cross-sectional dimensions of 2.4×1.2 m^2 ($W \times H$) following honeycombs, several screens, and a contraction ratio of 6.3:1. The side walls are made of transparent acrylic and the floor and ceiling have been fit with either glass or acrylic windows in select locations for PIV. The facility is capable of flow speeds up to 35 m s^{-1} and hotwire measurements have shown that the freestream turbulence intensity at the midpoint of the test section is consistently less than 0.4% when the speed is above 2 m s^{-1} (Johnson & Kostiuk 2000).

The elongated blunt body model was machined from an aluminum plate and sanded to a fine surface finish. It has a BTE height $h = 12.9$ mm and a chord length $c = 600$ mm, resulting in an aspect ratio of $AR = 46.5$. The leading edge was made semi-elliptical with a major to minor axis ratio of 5:1 to prevent leading edge flow separation, and 1 mm tripping wires were attached to the surface 105 mm downstream from the leading edge on both sides of the model to uniformly trigger transition along the span. In the case of laminar flow, the perturbation caused by the wire was not amplified. The model was oriented at zero angle of attack, spanning the entire 1.2 m from floor to ceiling to produce a blockage ratio of 0.5%. The elongated blunt body model can be viewed in figure 1.

2.2. *Two-Component Particle Image Velocimetry*

A 2C-PIV system was utilised in two configurations to measure instantaneous velocity fields of the upstream boundary layer in the x-y plane (denoted as FOV1) and the low-speed zones near the BTE in the x-z plane (denoted as FOV2). The illumination was provided by an Nd:YAG laser (Spectra-Physics, PIV-400-10) that is capable of outputting 532 nm light at 400 mJ per pulse with a pulse width of 5-8 ns. The laser beam was shaped using one negative cylindrical and two spherical lenses to produce a laser sheet with a thickness of 1 mm. The resulting laser sheet was then directed as necessary using several adjustable mirrors. Imager ProX-4M cameras were used to collect images, each featuring

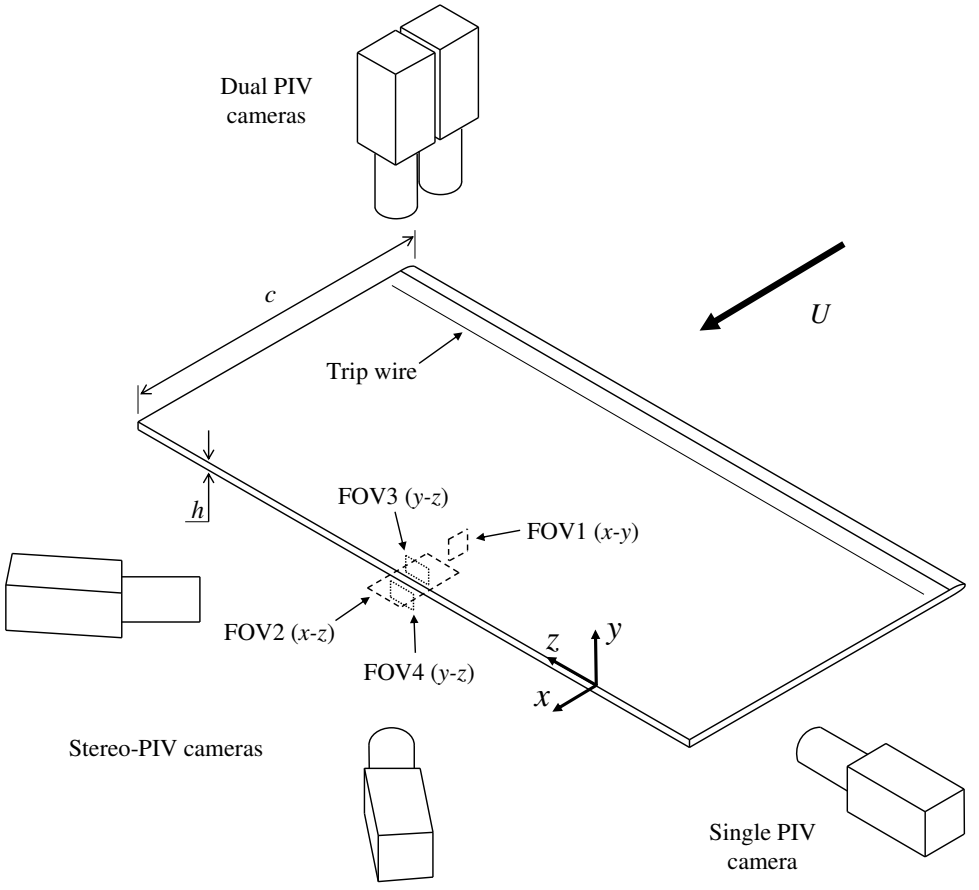

FIGURE 1. Schematic of the particle image velocimetry configurations and viewing regions. Note that $z = 0$ is located at centre span. The axis is offset here for clear viewing of the imaging planes. The model has a BTE height $h = 12.9$ mm and a chord length $c = 600$ mm.

a 2048×2048-pixel CCD sensor with a 7.4×7.4 μm^2 pixel size and 14-bit resolution. A schematic representation of the 2C-PIV setup is included in figure 1.

The boundary layer within FOV1 was imaged at a distance of $7h$ upstream from the BTE at centre span. A Nikon lens with a focal length of $f = 200$ mm and an aperture setting of $f/5.6$ was utilised with the camera which was set 0.7 m from the viewing plane, resulting in a digital resolution of 20.5 μm pix^{-1} and a streamwise-wall-normal FOV of $(\Delta x, \Delta y) = 42 \times 42$ mm^2 $(3.3h \times 3.3h)$. The flow was seeded with ∼1 μm particles using a fog generator, and then 500 double-frame images were collected at a frequency of 4 Hz for each flow speed considered.

The low-speed zones in the boundary layer and wake regions of the flow were measured using FOV2 in the x-z plane at $y = 1.5$ mm above the surface. Two cameras were fit with identical Nikon lenses, each with $f = 200$ mm and aperture settings of $f/8.4$. They were placed side by side at a distance of 1.3 m from the viewing plane. The digital resolutions of the upstream and downstream cameras were 34.4 and 34.2 μm pix^{-1}, respectively, and the viewing regions overlapped by 5 mm so that the resulting vector fields could be stitched together. The combined streamwise-spanwise FOV had dimensions of $(\Delta x, \Delta z)$

$= 135 \times 70$ mm^2 ($10.5h \times 5.4h$) centred at $x = 0$ and at centre span. After seeding with $\sim$1 μm fog particles, sets of 5000 double-frame images were collected by both cameras simultaneously at a frequency of 4 Hz for each flow speed considered.

The images were processed using DaVis 8.2 software (LaVision GmbH). First, a pre-processing step was necessary to improve image quality. The minimum of each ensemble was subtracted to remove background noise, followed by normalization using ensemble averages. FOV1 was imaged to obtain mean velocity profiles, and so an ensemble-of-correlation was applied to these sets (Meinhart *et al.* 2000). A multi-pass algorithm was used with 24×24-pixel (0.49×0.49-mm) interrogation windows with 75% overlap for the final pass. A 4:1 elliptical Gaussian distribution was applied to the window with the major axis of the ellipse in the streamwise direction to improve the correlation. FOV2 was processed using a standard multi-pass cross-correlation with the final passes utilizing Gaussian 48×48-pixel (1.65×1.65-mm) interrogation windows with 75% overlap. A postprocessing step was applied to the wake ensembles using universal outlier detection (Westerweel & Scarano 2005) and linear interpolation to account for incorrect and missing vectors, which made up less than 1% of each vector field.

2.3. *Stereoscopic Particle Image Velocimetry*

The wake and boundary layer regions were characterised using two different stereo-PIV systems. The first system utilises the same laser and cameras as the 2C-PIV experiments and the second is high-speed for collecting time-resolved images. The high-speed system makes use of a dual-cavity Nd:YLF laser (Photonics Industries, DM20-527-DH) at 527 nm with a maximum frequency of 10 kHz. The combined beam of the two laser cavities is capable of outputting a maximum of 40 mJ per pulse (at 1 kHz) with a pulse width of 170 ns. Two Phantom v611 high-speed cameras were utilised, each with a 1280×800-pixel CMOS sensor with a 20×20 μm^2 pixel size and 12-bit resolution. The first stereoscopic y-z viewing plane (denoted as FOV3) was located $0.3h$ upstream from the BTE location at centre span and began at the surface of the model ($y = 0$). The second stereoscopic y-z viewing plane (denoted as FOV4) was centred at $y = -0.5h$ and located $2h$ downstream from the BTE location as shown in figure 1.

Snapshots of the flow in FOV3 and FOV4 were captured for statistical analysis with higher spatial resolution. The mean flow direction is perpendicular to these viewing planes and so the second laser sheet pulse was moved 0.5 mm downstream from the first in both FOV3 and FOV4 to improve the number of common particles captured between frames. Each laser sheet pulse had a thickness of 1.5 mm using the same combination of optics as used previously, resulting in a total laser sheet thickness of 2 mm centred at $x = -0.3h$ for FOV3 and at $x = 2h$ for FOV4. The stereo-PIV cameras were each set approximately 1 m from the FOVs and were fit with Scheimpflug mounts and Nikon lenses with $f = 200$ mm. An aperture setting of $f/11$ was used on the forward scattering camera, while a setting of $f/8.4$ was used on the camera with a backward scattering orientation. A two-step stereoscopic calibration process was used for both FOVs which included a three-dimensional target calibration followed by self-calibration with a small set of particle images (Wieneke 2005). The spanwise-wall-normal FOV was (Δz, Δy) $= 76 \times 61$ mm^2 ($5.9h \times 4.7h$) with a digital resolution of 28.8 μm pix^{-1} and a residual error of 0.06 pix for FOV3. A spanwise-wall-normal FOV of (Δz, Δy) $= 75 \times 59$ mm^2 ($5.8h \times 4.6h$) with a digital resolution of 28.1 μm pix^{-1} and a residual error of 0.06 pix was obtained for FOV4. The flow was seeded with $\sim$1 μm particles using a fog generator and 5000 double-frame images were collected from each camera simultaneously at a frequency of 4 Hz for each flow speed considered and in both FOV3 and FOV4.

High-speed stereoscopic measurements were also conducted within FOV4 for the

purpose of studying the temporal evolution of the vortices in the wake. The laser sheet was made to be 2 mm thick using the same combination of optics as before. The high-speed cameras were placed in the same location as the Imager ProX cameras in the previous stereoscopic experiment and with the same lenses and aperture settings. The previously mentioned stereoscopic calibration procedure was followed, resulting in a spanwise-wall-normal FOV of $(\Delta z, \Delta y) = 115 \times 58$ mm^2 $(8.9h \times 4.5h)$ with a digital resolution of 71.6 μm pix^{-1} and a residual error of 0.02 pix. Ensembles of 5400 time-resolved images were collected at an acquisition frequency of 6.2 kHz for each flow speed considered.

All images were once again processed using DaVis 8.2. The double-frame stereo-PIV images were cross-correlated using multiple passes, the last of which utilised Gaussian 96×96-pixel (2.70×2.70-mm) interrogation windows with 75% overlap. A postprocessing step was then applied which removed and replaced outliers and interpolated missing vectors. The incorrect and missing vectors accounted for less than 4% of each vector field. The high-speed stereo-PIV images were processed using a sliding ensemble-of-correlation algorithm with a filter length of 5 images using 4 successive pairs each with a time separation of $\Delta t = 161$ μs to reduce random, high-frequency noise (Ghaemi *et al.* 2012). The operation utilised a multi-pass cross-correlation with final Gaussian 48×48-pixel (3.44×3.44-mm) interrogation windows with 75% overlap. No postprocessing was performed on the resulting time-resolved vector fields.

3. Results and Discussion

3.1. *Upstream Boundary Layer Development*

The mean boundary layer profiles $7h$ upstream from the BTE are presented on both linear and semi-logarithmic axes in figures $2a$ and $2b$, respectively. The high spatial resolution of the 2C-PIV measurements from the ensemble-of-correlation technique in FOV1 allowed for calculation of the inner layer scales, including the wall unit λ_0, by fitting a line to the linear viscous sublayer of the mean profiles. The state of the upstream boundary layer is summarised in table 1. By inspection of figure $2a$ and the calculated shape factors (H, the ratio of displacement thickness to momentum thickness) in table 1, it is evident that the upstream boundary layer is laminar for $Re(h) = 1900$ and 3500, transitional for $Re(h) = 5200$, and turbulent for $Re(h) = 7000$ and 8700.

It can be seen in figure $2b$ that the turbulent boundary layer profiles at $Re(h) = 7000$ and 8700 do not follow the standard logarithmic 'law of the wall' for a zero pressure gradient (ZPG) turbulent boundary layer. In fact, both turbulent profiles clearly exceed the logarithmic line. This deviation can be attributed to the favourable pressure gradient (FPG) caused by the low-pressure near-wake region of the body. This mean profile behaviour is typical of FPG turbulent boundary layers due to their tendency to accelerate and relaminarise, causing the semi-logarithmic profiles to shift towards the laminar curves (Patel & Head 1968; Badri Narayanan & Ramjee 1969; Blackwelder & Kovasznay 1972). This flow acceleration has been confirmed near the BTE using PIV measurements; however, the results have been omitted for brevity. The remainder of this investigation will only consider $Re(h) = 3500$, 5200, and 7000 as the laminar, transitional, and turbulent cases, respectively, to study the effect that a transitioning upstream boundary layer may have on the wake.

3.2. *Secondary Instability Wavelength*

The spanwise distance between adjacent counter-rotating streamwise vortex pairs within the wake region must be determined to characterise the secondary instability

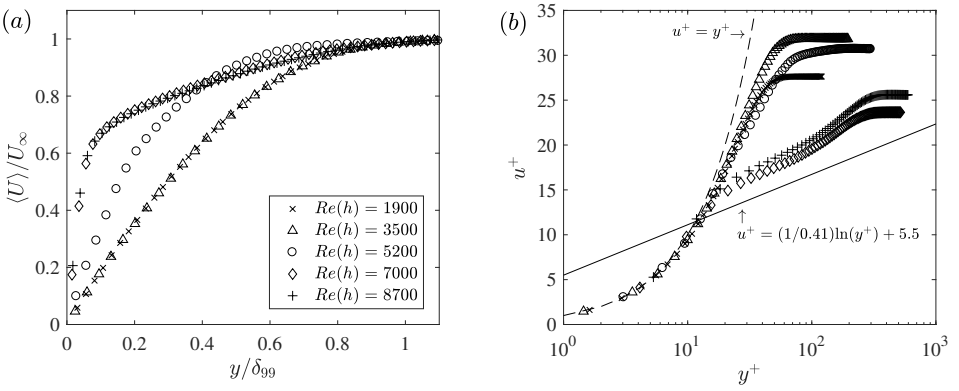

FIGURE 2. Mean velocity profiles $7h$ upstream of the BTE (FOV1) plotted using (*a*) linear and (*b*) semi-logarithmic axes. Both sets of profiles have been decimated by a factor of 2 to improve visibility of the data points. The direct overlap between laminar and turbulent profiles in (*a*) reveals that the flow is fully laminar at $Re(h) = 3500$ and fully turbulent at $Re(h) = 7000$. This is also concluded from the shape factors (H) provided in table 1.

$Re(h)$	$Re(L)$	U [m s^{-1}]	λ_0 [µm]	δ_{99} [mm]	δ^* [mm]	θ [mm]	H
1900	75000	2.3	187	9.8	3.3	1.3	2.49
3500	140000	4.3	115	7.0	2.3	0.9	2.54
5200	205000	6.3	76	8.3	1.8	0.8	2.14
7000	276000	8.4	44	12.0	2.0	1.3	1.50
8700	342000	10.4	38	11.4	1.9	1.3	1.50

TABLE 1. Parameters relating to the mean velocity profiles located $7h$ upstream from the BTE (from FOV1 in figure 1). Note that L is the length of the model up to where these parameters were evaluated.

modes. This distance is also known as the secondary instability wavelength as described previously and will be denoted as λ_z. The streamwise wake vortices have been identified from the stereoscopic snapshots of FOV4 using two-dimensional Q-criterion (Jeong & Hussain 1995), where the partial derivative terms have been evaluated using a second-order central differencing scheme. All vortices, which are specified as regions of flow with $Q > 0$, were assigned a direction of rotation using the sign of streamwise vorticity (ω_x), and all $Q < 0$ were discarded. This was done to facilitate identification of the counter-rotating vortex pairs from within the stereoscopic snapshots. Sample snapshots of the fluctuating component of streamwise velocity (u') and the corresponding modified Q-criterion ($Q' = \omega_x Q/|\omega_x|$) are provided in figure 3 for $Re(h) = 3500$, 5200, and 7000. These samples have been selected at instances when the stereo-PIV plane was cutting through one of the primary spanwise vortices to emphasise the location of the streamwise vortex pairs with respect to the primary vortex cores.

Figures 3*a* and 3*c* reveal a clear divide between positive and negative u' at $Re(h) = 3500$ and 5200. This divide occurs where the fluid has no out-of-plane motion with respect to the advecting frame of reference and is represented as a white line separating the red and blue regions of flow corresponding to positive and negative regions of u', respectively. The divide exists due to the rotation of the primary spanwise vortices, as they contain fluid moving both with ($u' > 0$) and against ($u' < 0$) the advecting frame of reference as the vortex moves downstream. In contrast, the isocontour of $u' = 0$ for $Re(h)$

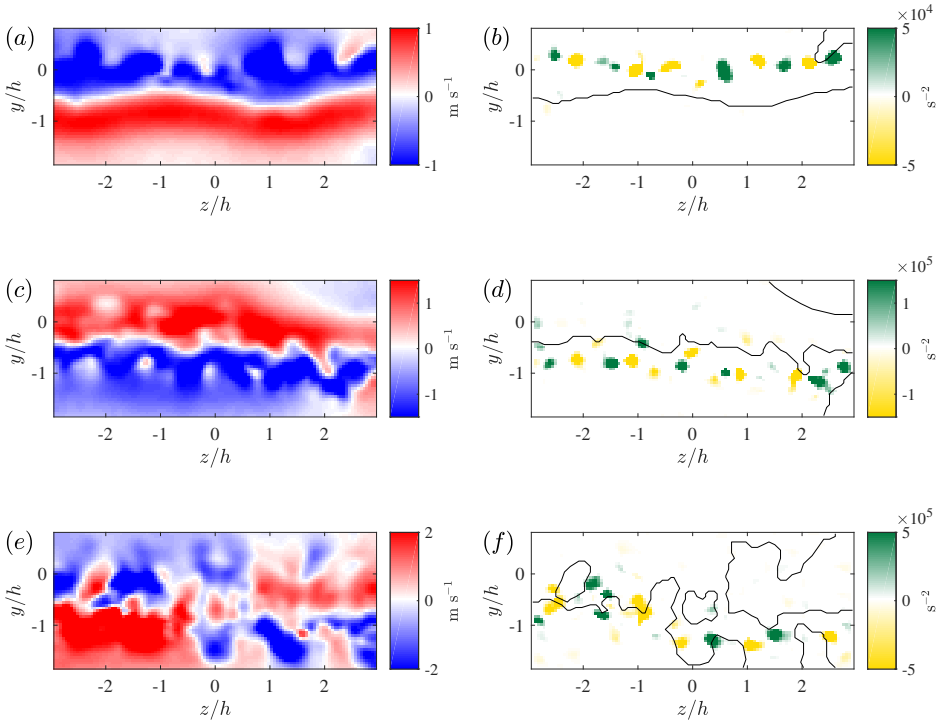

FIGURE 3. Instantaneous snapshots of the fluctuating component of streamwise velocity (u') and the corresponding modified Q-criterion ($Q' = \omega_x Q/|\omega_x|$) in the wake at $x = 2h$ for (a-b) $Re(h) = 3500$, (c-d) $Re(h) = 5200$, and (e-f) $Re(h) = 7000$. The $u' = 0$ lines have been added to the contour plots of Q' to facilitate comparison between plots. The streamwise vortex pairs tend to exist either on the $u' = 0$ line or in the region of the flow with $u' < 0$. The high-speed data within FOV4 have been used to create animations of the streamwise vortices visible in (b), (d), and (f). These videos can be found in the supplementary material as Movie 1, 2, and 3, respectively.

$= 7000$ in figure 3e is highly jagged with engulfed regions of opposite velocity fluctuation on either side of the wake centre line ($y = -0.5h$). This is caused by intense distortion of the primary spanwise vortices as Re increases. Distortion of the primary vortices can be found throughout the collected data and becomes more prevalent as Re is increased.

The counter-rotating streamwise vorticity pattern of the secondary instability is easily identified in the stereoscopic snapshots of Q' presented in figures 3b, 3d, and 3f. By comparison between the snapshots of u' and Q', it is evident that the streamwise vortices of the secondary instability tend to exist either on the $u' = 0$ line or in the region of the wake with $u' < 0$. As previously mentioned, the latter corresponds to the portion of the primary spanwise vortex that is rotating upstream with respect to the advecting frame of reference. This streamwise vortex placement persists when the wake is distorted as can be seen in figure 3f. The jagged interface between positive and negative u' brings a similar jaggedness to the spanwise sequence of secondary vortices, with the streamwise vortices continuing to exist either on the $u' = 0$ line or in the region with $u' < 0$. This behaviour of secondary vortex pairs is consistent with the simplified mode B model that has been proposed by Brede *et al.* (1996) for the cylinder wake. Their model features simply connected streamwise vortex tubes which weave between primary spanwise vortices, always passing around the side of the primary vortex that is rotating

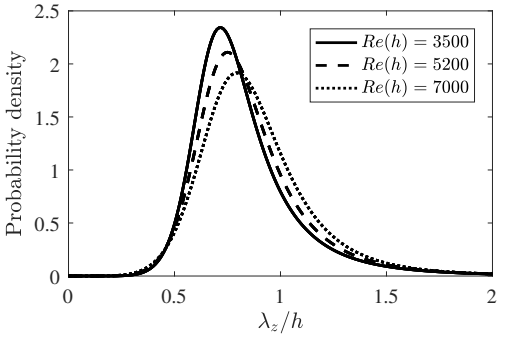

FIGURE 4. Probability density functions of secondary instability wavelength (λ_z) in the wake at $x = 2h$ for $Re(h) = 3500$, 5200, and 7000. The wavelengths were obtained by spatial correlation of vortex cores identified using a modified Q-criterion ($Q' = \omega_x Q/|\omega_x|$) as described by equation 3.1.

towards the upstream direction. The streamwise vortices alternate sign in the spanwise direction, therefore existing in counter-rotating pairs, and have a secondary instability wavelength of approximately $1d$ as determined by their experiments. A similar model has been given by Williamson (1996*a*); however, the author stated that it was not obvious that the streamwise vortices were simply connected.

The spanwise distance between adjacent streamwise vortex pairs in the present stereoscopic snapshots has been calculated using a spatial autocorrelation in the spanwise direction. The operation has been applied to the snapshots of Q'. The autocorrelation coefficient of the i^{th} snapshot shifted in the spanwise direction by Δz is given by

$$C(\Delta z) = \frac{\langle Q'(y_0, z_0, t_i) \cdot Q'(y_0, z_0 + \Delta z, t_i) \rangle}{Q'_{rms}(y_0, z_0, t_i) Q'_{rms}(y_0, z_0 + \Delta z, t_i)} \tag{3.1}$$

where the subscript *rms* denotes the root-mean-square operation. The distance between adjacent vortex pairs within each snapshot was then taken to be twice the distance between the initial maximum value ($C(0) = 1$) and the first minimum of the respective autocorrelation. This minimum occurs when the snapshot has been shifted such that vortices with opposite signs align, and therefore it represents a distance that is half that of the secondary instability wavelength.

The process described above has been applied to all stereo-PIV ensembles. Probability density functions (PDFs) that have been fit to the resulting values of λ_z using a Burr type XII distribution (Tadikamalla 1980) are shown in figure 4. By inspection, each PDF of λ_z is unimodal and slightly right-skewed. The peaks represent estimates for the most probable values of λ_z and correspond to $0.72h$, $0.75h$, and $0.79h$ for $Re(h)$ = 3500, 5200, and 7000, respectively. These values for λ_z closely match the secondary instability wavelength of mode B found in the wakes of cylinders (Williamson 1996*b*) and the predicted wavelength of mode S′ for the wake of an elongated blunt body (Ryan *et al.* 2005). The distributions do not change significantly as the flow upstream from the BTE transitions from laminar to turbulent; however, a reduction in magnitude and shift of the peak to the right is visible. Each distribution being unimodal suggests that there is only one dominant mode in the wake for the investigated Re. Additionally, any dominant presence of the BTE mode B′ in the wake can be ruled out, as it has a secondary instability wavelength closer to $2.2h$.

3.3. *Temporal Behaviour of the Streamwise Wake Vortices*

The organisation of the streamwise vortices in the wake must be determined to further characterise the secondary instability. In particular, knowledge of how the vortices relate from one primary shedding cycle to the next is required to distinguish between the cylinder mode B and the BTE mode S′. The two modes have similar fine-scale spanwise wavelengths; however, the mode B secondary vortices maintain their direction of rotation over many shedding cycles while the mode S′ secondary vortices change their direction of rotation between each cycle of the primary instability (Ryan *et al.* 2005). In the previous subsection, it was determined that the most probable secondary instability wavelength for the *Re* considered here is approximately $\lambda_z = 0.7\text{-}0.8h$. How the secondary vortices behave between primary shedding cycles is the last piece of information required to determine which mode is present in the wake.

High-speed stereo-PIV measurements have been performed within FOV4 at $x = 2h$ and the resulting time-resolved sequences of vector fields have been used to investigate the temporal characteristics of the streamwise wake vortices. The modified Q-criterion ($Q' = \omega_x Q/|\omega_x|$) has been determined as described in section 3.2 to identify the streamwise vortex pairs within each stereoscopic velocity field. The resulting time-resolved evolution of Q' has been obtained by stacking the two-dimensional plots along the third dimension (i.e. time) to facilitate visualization of the vortical structures as they evolve temporally. Isosurface constructions of the vortical structures within the wake at $x = 2h$ are given in figure 5 for $Re(h) = 3500$ and 7000. These plots are representative of the wake behaviour contained in all high-speed data collected in this study.

The alternating sign of vorticity in the spanwise direction is highly visible in the isosurface constructions in figure 5. Additionally, it is straightforward to see by visual inspection that many of the streamwise vortices in figure 5*a* maintain their direction of rotation over the primary shedding cycles presented in the figure. This is not as easily visualised at higher *Re* when the wake region becomes more turbulent and three-dimensional. Thus, visual inspection of the vortex samples needs to be verified by statistical analysis. This has been done using a spatial cross-correlation in the spanwise direction, applied to the reconstructed temporal evolution of Q'. Subsequent vortex shedding cycles have been isolated as three-dimensional matrices and cross-correlated to determine whether the vortices change their direction of rotation between primary cycles. If the vortices maintain their rotational directions, the cross-correlation coefficient will begin at a positive value at $\Delta z = 0$ and trend towards a minimum with increasing Δz. This minimum will occur at a value of roughly $\Delta z = \lambda_z/2$ due to the alignment of vortices with opposite directions of rotation after the shift. However, the opposite will be true if the vortices are to change rotational direction between primary shedding cycles, i.e. the cross-correlation coefficient will begin at a minimum due to the alignment of vortices with opposite rotation and trend towards a maximum value at the location $\Delta z = \lambda_z/2$ where the vortices with the same rotational direction now align. This process has been applied to all N vortex shedding cycles for each *Re* considered and the resulting cross-correlation curves have been averaged. The mathematical description of the operation is given by

$$\rho(\Delta z) = \frac{1}{N-1} \sum_{i=1}^{N-1} \frac{\langle Q'(y_0, z_0, t_i) \cdot Q'(y_0, z_0 + \Delta z, t_i + T_{shed}) \rangle}{Q'_{rms}(y_0, z_0, t_i) Q'_{rms}(y_0, z_0 + \Delta z, t_i + T_{shed})} \tag{3.2}$$

where T_{shed} is the period of the primary vortex shedding cycle and Q' is a three-dimensional matrix containing a complete shedding cycle. The results for $Re(h) = 3500$, 5200, and 7000 are given in figure 6. In agreement with the instantaneous visualizations in figure 5, the averaged cross-correlation curves reveal that the streamwise vortices

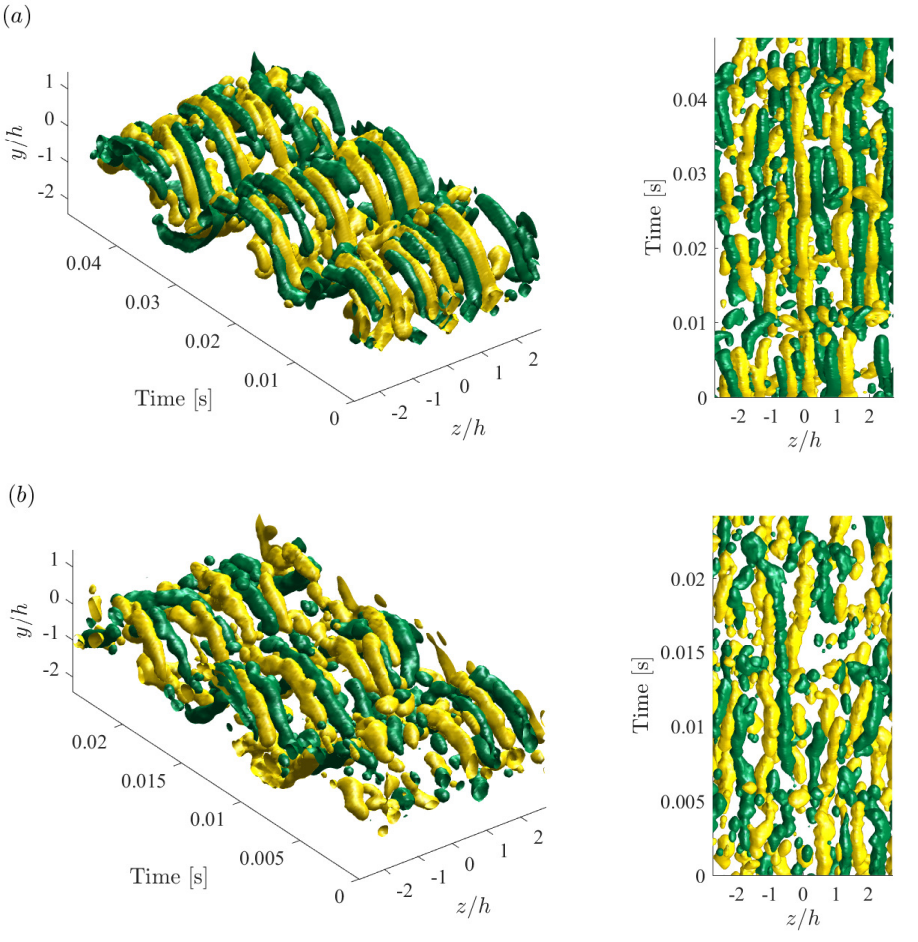

FIGURE 5. Isosurface constructions of modified Q-criterion ($Q' = \omega_x Q/|\omega_x|$) in the wake at $x = 2h$ for (*a*) $Re(h) = 3500$ (isosurface at $Q' = \pm 2000$ s^{-2}) and (*b*) $Re(h) = 7000$ (isosurface at $Q' = \pm 18000$ s^{-2}). Green and gold represent positive and negative rotational directions, respectively. Isosurface values have been chosen to obtain clear visualizations. Lowering the value makes the plots denser but does not alter the patterns displayed. Note that a second-order regression filter with a kernel size of 5 has been applied to the data to reduce noise and facilitate visualization.

maintain their direction of rotation during primary shedding cycles since a maximum peak is observed at $\Delta z = 0$. Moreover, the first minimum in each plot occurs at about $\Delta z/h = 0.5$, confirming that the mean secondary instability wavelength is near $\lambda_z = 1h$ for the considered Re and therefore matches that of the cylinder mode B.

Upon further inspection of the isosurface constructions in figure 5, it is evident that the streamwise vortices maintain their spanwise positions over time. This behaviour agrees with the models proposed by Brede *et al.* (1996) and Williamson (1996*a*) for the circular cylinder mode B; however, the behaviour contradicts the model proposed by Naghib-Lahouti *et al.* (2012) for the secondary instability in the wake of an elongated blunt body at a smaller AR of 12.5 based on LIF visualizations and reconstructed velocity fields. Their blunt body model contains streamwise vortices which stagger their spanwise positions every half shedding cycle, which is not observed here. Moreover, the streamwise

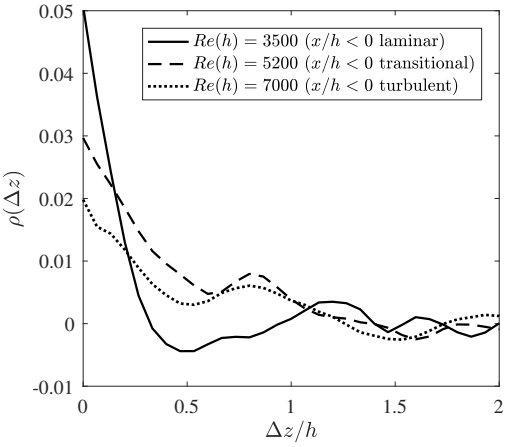

FIGURE 6. Average of spanwise cross-correlations applied to three-dimensional modified Q-criterion ($Q' = \omega_x Q/|\omega_x|$) between all subsequent primary vortex shedding cycles following equation 3.2. All cross-correlation curves begin at a maximum positive value, indicating that the vortex pairs maintain their directions of rotation during primary shedding cycles. The first minimum of each curve is near $\Delta z/h = 0.5$, providing further evidence that the secondary instability wavelength is close to $\lambda_z = 1h$.

vortices in figure 5*a* appear to be simply connected as modelled by Brede *et al.* (1996), although it is difficult to confirm whether this behaviour is persistent in the wake.

Thus far, all results presented regarding the secondary wake vortices suggest that the cylinder mode B is the dominant secondary instability within the wake of the elongated blunt body studied here with $AR = 46.5$ for $Re(h) = 3500$, 5200, and 7000. No evidence of the BTE mode B$'$ nor S$'$ has been found within the collected data as was anticipated from the stability analysis of Ryan *et al.* (2005) for $2.5 \leqslant AR \leqslant 17.5$ and a maximum $Re(h)$ of 700 and the experimental work of Naghib-Lahouti *et al.* (2012, 2014) for $AR = 12.5$ and $250 \leqslant Re(h) \leqslant 5 \times 10^4$, although we would like to emphasise the large differences in AR between these studies and the present investigation. The visual inspection and spatial-correlation analysis of both the time-resolved and statistical stereo-PIV data have been used to reach this conclusion.

3.4. *Low-Speed Zones of Streamwise Velocity*

Both the upstream boundary layer and the wake region feature low-speed zones of streamwise velocity fluctuation. In the boundary layer they are often referred to as streaks due to their streamwise elongation, and they exist when the flow is turbulent or transitioning to turbulence. The boundary layer streaks are directly related to streamwise vortices near the wall (Blackwelder & Eckelmann 1979; Schoppa & Hussain 2002; Tomkins & Adrian 2003), and the spanwise distance between adjacent low-speed streaks in a ZPG turbulent boundary layer ranges from 90 to 140 wall units depending on the distance from the wall (Smith & Metzler 1983; Lin *et al.* 2008). As previously mentioned, low-speed zones of streamwise velocity also exist in the wake when secondary instabilities are present and the spanwise distance between adjacent low-speed zones matches the secondary instability wavelength (λ_z) in the wake (Mansy *et al.* 1994; Wu *et al.* 1996). The low-speed zones in the boundary layer and wake regions and their respective vorticity content will be investigated in this section. The spanwise distance between adjacent low-speed zones will be denoted as Λ_z.

Sample snapshots of the fluctuating component of streamwise velocity (u') are given in figure 7 for $Re(h) = 3500$, 5200, and 7000 from the stitched 2C-PIV measurements within FOV2. The respective laminar, transitional, and turbulent nature of the upstream flow ($x < 0$) is evident within these snapshots. The fluctuation in streamwise velocity is almost non-existent in the upstream boundary layer in figure 7*a*, as is expected for laminar flow. Conversely, the well-known turbulent boundary layer streaks are highly visible in figure 7*c*, where both low- and high-speed streaks can be seen to have a continuous presence. The transitional nature of the flow in figure 7*b* is also evident, as boundary layer streaks are visible but do not populate the entire snapshot. Additionally, spanwise bands of low- and high-speed fluid are visible in the wake region ($x > 0$) of all snapshots. These bands represent slices through the primary spanwise vortices, resulting in low- and high-speed components which stem from the primary vortices that are rotating against and with the advecting frame of reference. The high-speed spanwise bands therefore represent primary vortices that have rolled off the near-side of the BTE ($y = 0$) and the low-speed spanwise bands represent primary vortices that have rolled off the far-side ($y = -h$). The undulation of streamwise velocity in the spanwise direction (within the bands) is visible in all three snapshots, although it is more pronounced in the spanwise bands that have $u' < 0$. This is consistent with the snapshots presented in figure 3, which revealed that the streamwise vortex pairs exist within the portion of each spanwise vortex that is rotating against advecting frame of reference (i.e. $u' < 0$). This once again agrees with the cylinder mode B models that have been presented by Brede *et al.* (1996) and Williamson (1996*a*) and explains why the same undulating patterns are not visible in the spanwise bands with $u' > 0$.

The spanwise distance between adjacent low-speed streaks in the upstream boundary layer was calculated using a spatial autocorrelation similar to the one described in section 3.2 and presented in equation 3.1. However, in the wake, the autocorrelation was only applied to the spanwise bands with $u' < 0$ that hold the undulating patterns. These bands do not have a continuous presence in a single streamwise location, and so a window of streamwise width h (the height of the BTE) was used to search for the low-speed bands within each snapshot. The window was moved in the streamwise direction along the snapshots and the window with a minimum average velocity with respect to the rest of the snapshot was selected. The spanwise autocorrelation operation was applied to each window that was selected. The distance between adjacent low-speed zones was taken to be twice the distance between the initial maximum of the autocorrelation and the first minimum, and the centre of the window was considered the streamwise location of each corresponding autocorrelation result. The results were then binned at varying streamwise locations. The estimated Λ_z in both the upstream boundary layer and wake have been fit with PDFs which are given in figure 8 for $Re(h) = 3500$, 5200, and 7000 and at various streamwise locations before and after the BTE. The PDFs were estimated using a Burr type XII distribution (Tadikamalla 1980).

Similarly to the PDFs of λ_z in figure 4, all distributions of Λ_z in figure 8 are unimodal and right-skewed. The peaks of the upstream boundary layer distributions (figures 8*a-c*) are more distinct than those of the wake (figures 8*d-f*), and it is generally observed that an increase in streamwise location brings a reduction in magnitude and shift of the peaks to the right. The most probable value for Λ_z in the upstream turbulent boundary layer at $Re(h) = 7000$ is approximately $0.41h$ based on the peaks of the PDFs at $x = -2h$ and $-h$ given in figures 8*a* and 8*b*, respectively. Using the wall unit at $x = -7h$ presented in table 1 for $Re(h) = 7000$ ($\lambda_0 = 44$ μm), this distance corresponds to $120\lambda_0$. This approximation falls within the expected range of 90-$140\lambda_0$ for a ZPG turbulent boundary layer (Smith & Metzler 1983; Lin *et al.* 2008), despite the FPG in this boundary layer. Using table

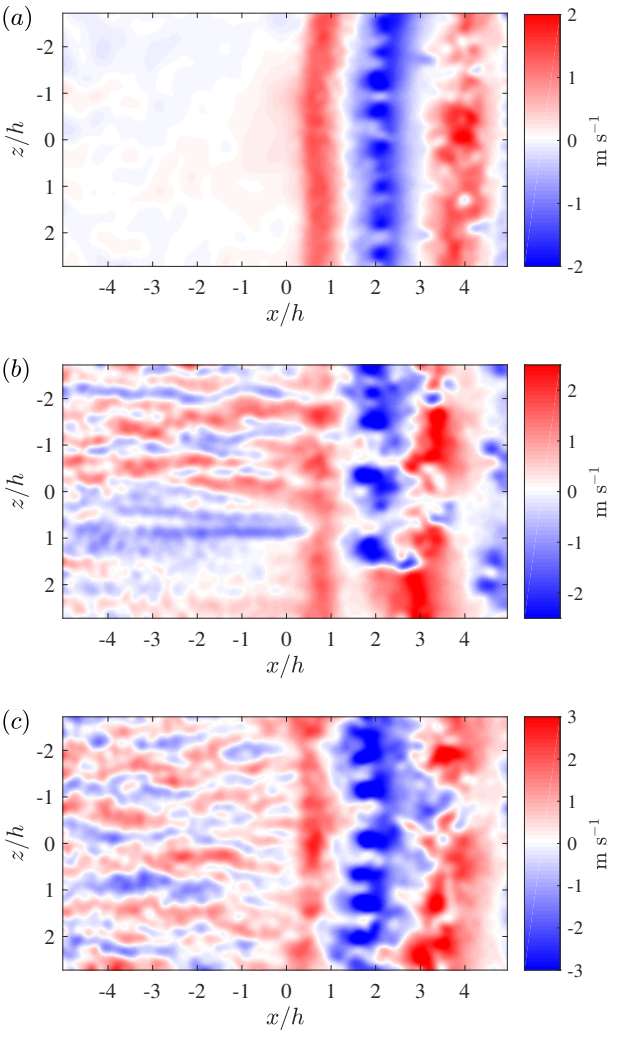

FIGURE 7. Instantaneous fluctuating component of streamwise velocity (u') in the x-z plane (y = 1.5 mm) for (a) $Re(h) = 3500$, (b) $Re(h) = 5200$, and (c) $Re(h) = 7000$. The BTE is located at $x = 0$, and $x < 0$ represents the upstream boundary layer while $x > 0$ represents the wake. The respective laminar, transitional, and turbulent states of the upstream boundary layers are evident in the snapshots. The spanwise bands of positive and negative u' in the wake represent the primary von Kármán vortices.

1 and the peaks in figures 8a and 8b, the most probable value for Λ_z in the transitional boundary layer at $Re(h) = 5200$ is $81\lambda_0$.

The PDFs for Λ_z in the wake at $x = 2h$ (figure 8e) are similar to the distributions for λ_z at the same location (figure 4). The most probable values for these distributions are compared in table 2, where it can be seen that the differences between λ_z and Λ_z at $Re(h) = 3500$, 5200, and 7000 are relatively small and correspond to -5.6%, 3.1%, and 8.0%, respectively, indicating that there is in fact a relationship between λ_z and Λ_z. The power spectral density (PSD) of u' at $x = 2h$ has also been determined to further investigate Λ_z in the wake and to validate the results of the autocorrelations, as the latter may have filtered out wavelengths with lower energy content. The central spanwise rows

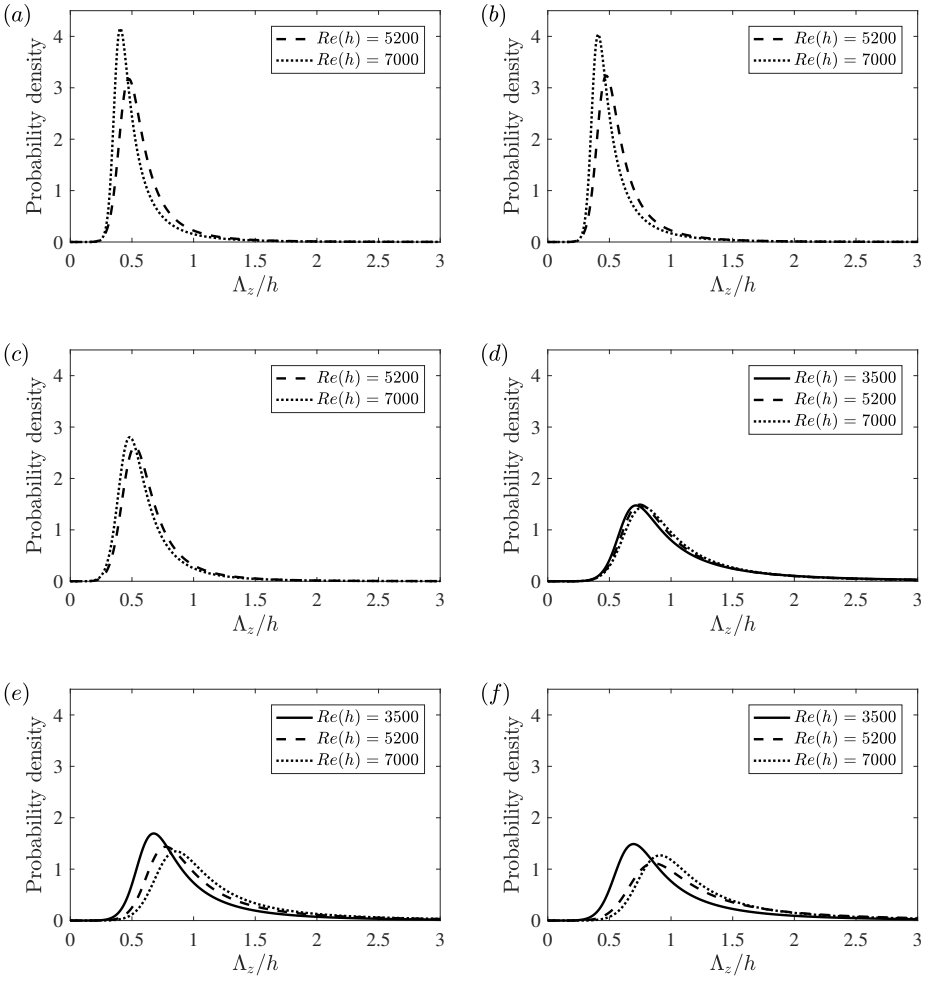

FIGURE 8. Probability density functions of the distance between adjacent low-speed zones (Λ_z) at $Re(h) = 3500$, 5200, and 7000 at streamwise locations (*a*) $x = -2h$, (*b*) $x = -h$, (*c*) $x = 0$, (*d*) $x = h$, (*e*) $x = 2h$, and (*f*) $x = 3h$. The peak of each distribution represents the most probable value for Λ_z at the corresponding streamwise location and Re.

of u' have been extracted from the conditionally sampled spanwise bands of negative u' (the same windows that were autocorrelated to create the PDFs in figure 8*e*). The data were multiplied with a Hanning window before PSD was calculated using a fast Fourier transform. The resulting spectrums have been averaged and presented in figure 9 as PSD versus normalised wavenumber (h/Λ_z). Each of the three spectrums features two peaks at the same locations for each Re. The first and second peaks correspond to $\Lambda_z = 5.4h$ and $1.1h$, respectively. The first value for Λ_z matches the total spanwise length of FOV2 and is therefore not physical. The second value of $\Lambda_z = 1.1h$ is close to the spanwise distances reported by the autocorrelations, thus validating the previous results. The absence of any other physical peak in the spectrums strengthens the observation that the cylinder mode B is the only secondary instability present in the wake of the elongated blunt body studied here.

The most probable values from all PDFs in figure 8 are plotted as a function of distance

$Re(h)$	λ_z	Λ_z
3500	$0.72h$	$0.68h$
5200	$0.75h$	$0.77h$
7000	$0.79h$	$0.86h$

TABLE 2. Most probable values for secondary instability wavelength (λ_z) and the spanwise distance between low-speed zones (Λ_z) in the wake at $x = 2h$ from the distributions given in figures 4 and 8*e*, respectively.

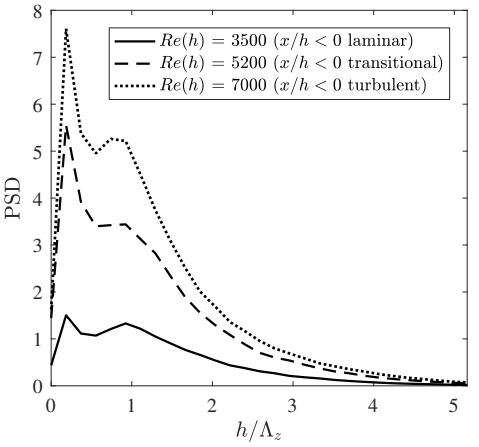

FIGURE 9. Power spectral densities of the spanwise signals of streamwise velocity fluctuation (u') in the wake at $x = 2h$ for $Re(h) = 3500$, 5200, and 7000. The first peak corresponds with the spanwise size of FOV2 and is therefore not physical. The second peak represents the secondary instability wavelength.

from the BTE ($x = 0$) in figure 10. This has been done to facilitate characterisation of the evolution of the low-speed structures as they move from the upstream boundary layer and into the wake. Figure 10 reveals that the boundary layer streak spacing remains relatively constant before a rapid increase in Λ_z over the range $0 < x < h$ as the low-speed structures of the boundary layer are replaced by those of the unsteady wake. Beyond $x = h$, Λ_z stays relatively constant for $Re(h) = 3500$ and continues to gradually increase for $Re(h) = 5200$ and 7000.

As mentioned previously, the low-speed zones of streamwise velocity in both the upstream boundary layer and wake are related to the streamwise vorticity field. Whether the streamwise vortices present in the upstream boundary layer re-organise into the secondary wake vortices or are replaced altogether has been investigated using the stereo-PIV snapshots in the boundary layer at $x = -0.3h$ (FOV3) and the wake at $x = 2h$ (FOV4). Two-dimensional Q-criterion (Jeong & Hussain 1995) has been used to identify vortices in the snapshots using a threshold to discard noise in the free-stream ($Q = 3000$ s^{-2} was chosen by inspection of numerous snapshots of Q). The absolute values of streamwise vorticity ($|\omega_x|$) in the conditionally selected vortex cores with $Q > 3000$ s^{-2} were summed and divided by the total area of the vortices to obtain a measure of average vorticity per unit vortex area within each snapshot. The results have been fit with PDFs using a Burr type XII distribution (Tadikamalla 1980) and are displayed in figure 11. The average vorticity content per unit area in the wake is nearly an order

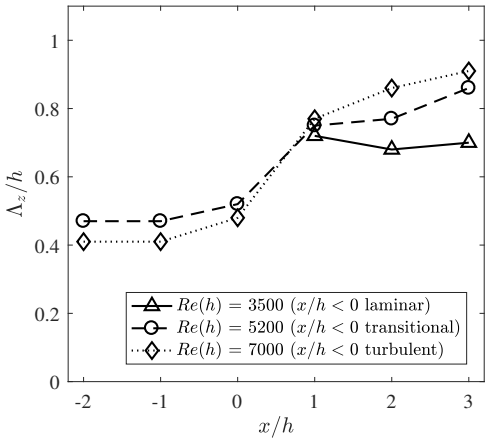

FIGURE 10. Most probable distance between adjacent low-speed zones (Λ_z) as a function of distance from the BTE ($x = 0$) for $Re(h) = 3500$, 5200, and 7000. Each point represents the peak of the corresponding probability density functions given in figure 8. The rapid change in Λ_z over the region $0 < x/h < 1$ is due to the boundary layer structures being replaced by the secondary instability.

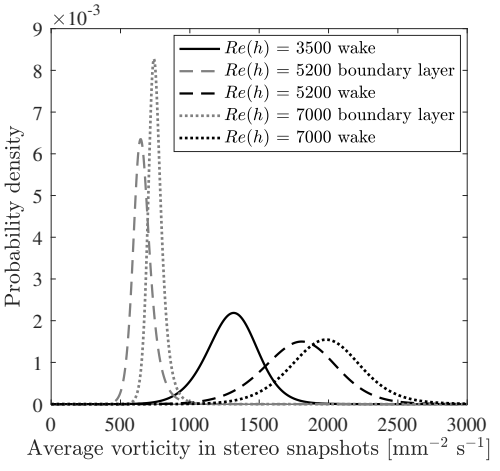

FIGURE 11. Probability density functions of average streamwise vorticity ($\langle\omega_x\rangle$) per unit area of the conditionally sampled vortex cores with $Q > 3000$ s^{-2} in the boundary layer at $x = -0.3h$ and wake at $x = 2h$ for $Re(h) = 3500$, 5200, and 7000. A change in vortex strength of nearly an order of magnitude is visible between the boundary layer and wake.

of magnitude higher than in the upstream boundary layer. This provides evidence to suggest that the mechanisms of streamwise vortex formation in the two flows are likely unrelated. This information, when coupled with the sharp increase in Λ_z over the range $0 < x < h$ observed in figure 10 and the fact that the secondary instability does not change significantly as the upstream boundary layer transitions from laminar to turbulent, is evidence that the structures in the upstream transitional and turbulent boundary layers evolve into the near-wake flow without having much impact on the wake organisation.

3.5. *The Proper Orthogonal Decomposition of Streamwise Velocity in the Wake*

Proper orthogonal decomposition (POD) is commonly used in turbulence studies to reduce flow fields to simplified representations (Berkooz *et al.* 1993). An ensemble is decomposed into time-varying amplitudes and a set of modes with decreasing energy content. The ensemble can be reconstructed using a select number of the modes to achieve a reduced-order representation of the data. The use of POD on snapshots of the fluctuating component of streamwise velocity (u') in the x-z plane of the wake is investigated in this section. This is done to study the energy content of the secondary instability in the wake and to carry out characterisation of the secondary instability wavelength (λ_z) using the POD-based method applied by Naghib-Lahouti *et al.* (2012, 2014). This comparison is primarily motivated by the differences in the wake structures reported between these studies and the present investigation, as it is not clear if the differences are physical or an artifact of the analysis techniques used. The present investigation has determined λ_z by direct measurement of the secondary vortices; however, Naghib-Lahouti *et al.* (2012, 2014) relied on measurements of u' in the streamwise-spanwise plane and therefore the measurements of λ_z were indirect.

The POD of u' by the method of snapshots (Sirovich 1987) has been performed on the snapshots within FOV2 ($x > 0$ only, i.e. just the wake) for $Re(h) = 3500$, 5200, and 7000. The first 8 POD modes and their energy content are given in figures 12 and 13, respectively. The first two POD modes for each Re capture the dynamics of the primary instability, and modes 3 and 4 capture its large-scale distortion. These first 4 POD modes contain large fractions of the energy in the flow with respect to the remaining modes as shown in figure 13. It is not clear if modes 5-8 are related to the distortion of the primary instability or the spanwise modulation of the secondary instability if λ_z is not known *a priori*. Figure 13 also reveals that the energy captured within the initial POD modes shifts to the higher modes as Re increases. As it is expected, it becomes increasingly difficult to capture the complete dynamics of the flow using only a few modes when the levels of turbulence increase. Additionally, the first 8 POD modes presented here are in agreement with those given by Naghib-Lahouti *et al.* (2014), and 6 of the modes for each Re are practically identical between studies.

The snapshots of u' have been reconstructed using varying numbers of modes and the same autocorrelation analysis used in section 3.4 to determine the distance between adjacent low-speed zones (Λ_z) in the wake has been performed on the reduced-order ensembles. This was done to investigate the impact that the POD of u' has on the PDFs of Λ_z. The effect of using 16, 24, 32, and 48 modes to reconstruct the snapshots of u' was investigated. These four cases cover the analyses of Naghib-Lahouti *et al.* (2012, 2014), which used either 32 POD modes or enough modes to retain at least 70% of the energy in the flow. This energy criterion was met by using 16-32 modes depending on Re in the latter case. Figure 14 displays the impact of these reconstructions on the PDFs of Λ_z in the wake at $x = 2h$ for $Re(h) = 3500$, 5200, and 7000. Note that a kernel technique was necessary for estimating the PDFs once the distributions became multimodal (Sheather 2004).

The PDFs in figure 14 show that the distributions of Λ_z are highly sensitive to how many modes are used to reconstruct the snapshots. In general, using fewer modes causes the peak of each distribution to decrease in magnitude and shift to the right, thus erroneously increasing the estimated values for λ_z. When 24 modes are used for reconstruction, the PDFs become multimodal with the first peak bearing some resemblance to the expected peak for λ_z. The peaks following the first one likely represent the wavelengths present in some of the more energetic modes, for example modes 3 and

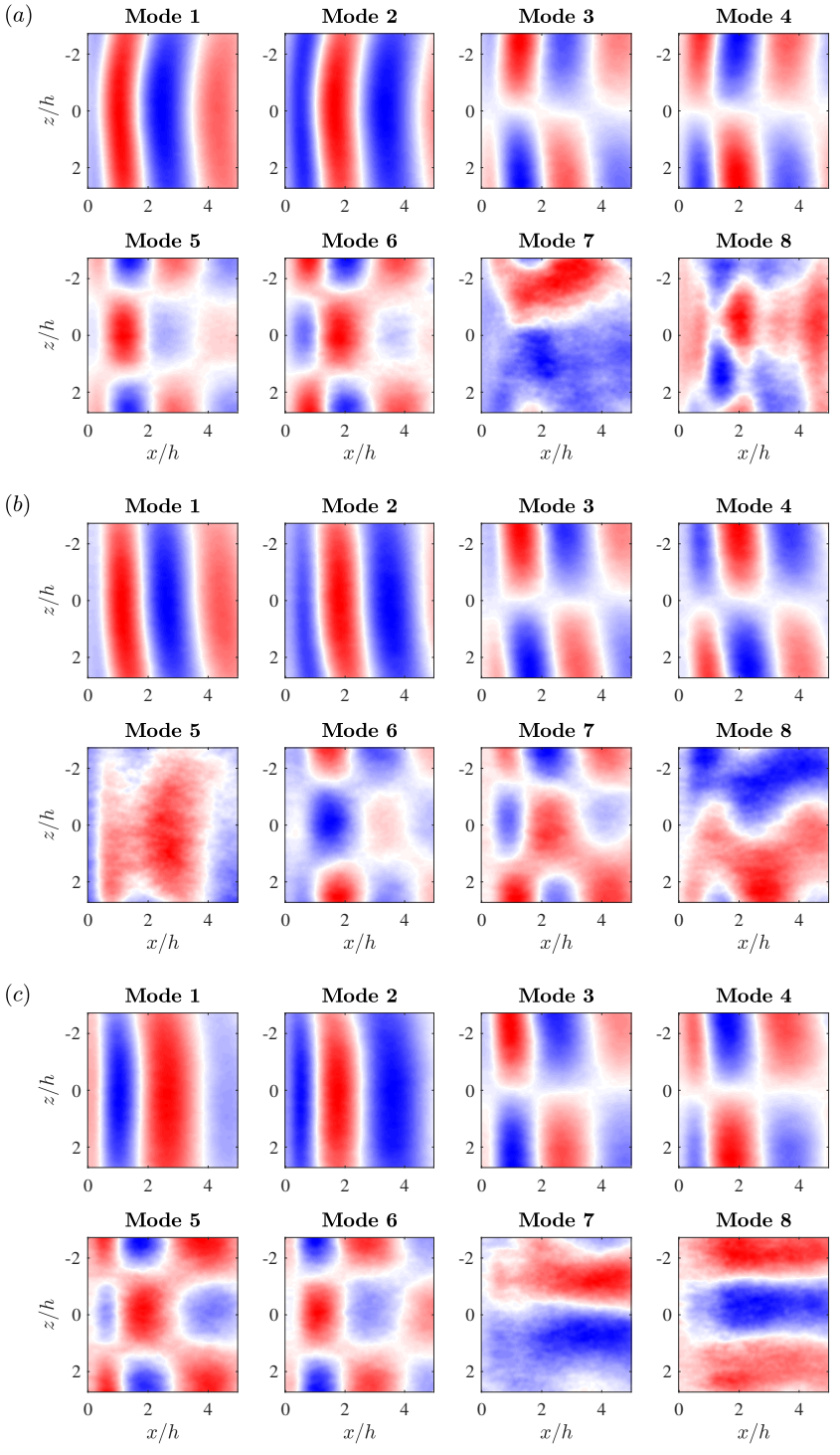

FIGURE 12. The first 8 POD modes of the fluctuating component of streamwise velocity (u') in the wake at $y = 1.5$ mm for (a) $Re(h) = 3500$, (b) $Re(h) = 5200$, and (c) $Re(h) = 7000$. The secondary instability wavelength is not visible in any of the modes.

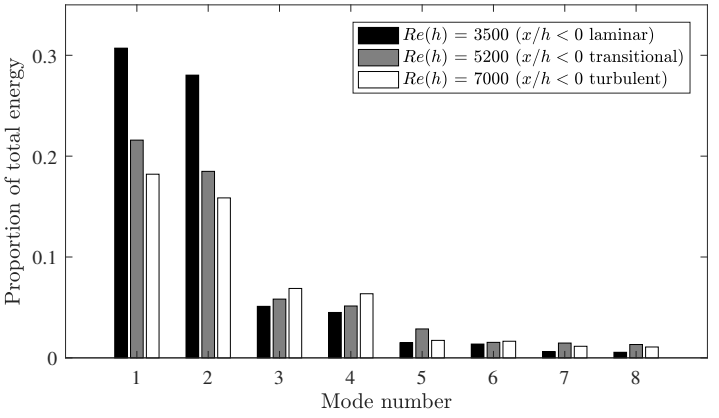

FIGURE 13. Energy associated with each of the POD modes given in figure 12. A shift in energy to the higher modes occurs as Re is increased, indicating higher levels of turbulence.

6 for any Re in figure 12. When 16 modes are used for reconstruction, the presence of the first distinct peak that represents λ_z is no longer dominant, suggesting that the majority of information regarding the secondary instability is stored beyond mode 16.

It is evident that the application of POD to streamwise-spanwise snapshots of u' when determining λ_z is highly dependent on the number of POD modes used to reconstruct the data ensembles and must be carefully applied. For example, when using 48 modes to reconstruct u' and thus preserving at least 70% of the energy in the flow as was done by Naghib-Lahouti *et al.* (2014), the mean values for Λ_z in the wake are $2.24h$, $2.21h$, and $2.26h$ for $Re(h) = 3500$, 5200, and 7000, respectively. These values nearly exactly match λ_z for the mode B′ instability predicted by Ryan *et al.* (2005) and fall within the range of mean values reported by Naghib-Lahouti *et al.* (2012, 2014). When the original snapshots are used (100% energy), the mean values are $1.01h$, $1.21h$, and $1.29h$, respectively, and are consistent with the direct measurements of the secondary vortices in the present study. There are large differences in AR between these studies and the present investigation, and so this does not dismiss the presence of mode B′ for small AR; however, a re-evaluation of the wavelength of the secondary instability and the formation of mode B′ for elongated blunt bodies with AR smaller than what is considered here is suggested.

4. Summary and Conclusions

The present experimental investigation utilised various PIV measurements to characterise the secondary instability in the wake of an elongated blunt body with $AR = 46.5$ at $Re(h) = 3500$, 5200, and 7000, and investigated its relationship with low-speed streamwise velocity patterns in both the upstream boundary layer and wake region. The wake was found to be populated with streamwise counter-rotating vortex pairs that are typical of bluff body wake flows. The most probable spanwise distance between adjacent vortex pairs in the wake at $x = 2h$ was found to range from 0.7-0.8h depending on Re. The streamwise vortices maintained both their rotational directions and spanwise positions during primary vortex shedding cycles. Furthermore, the secondary vortices appeared to be simply connected between cycles and were shown to wrap around the primary spanwise vortex cores while passing through the portion of each primary vortex that is rotating against the advecting frame of reference. The characteristics of the secondary instability

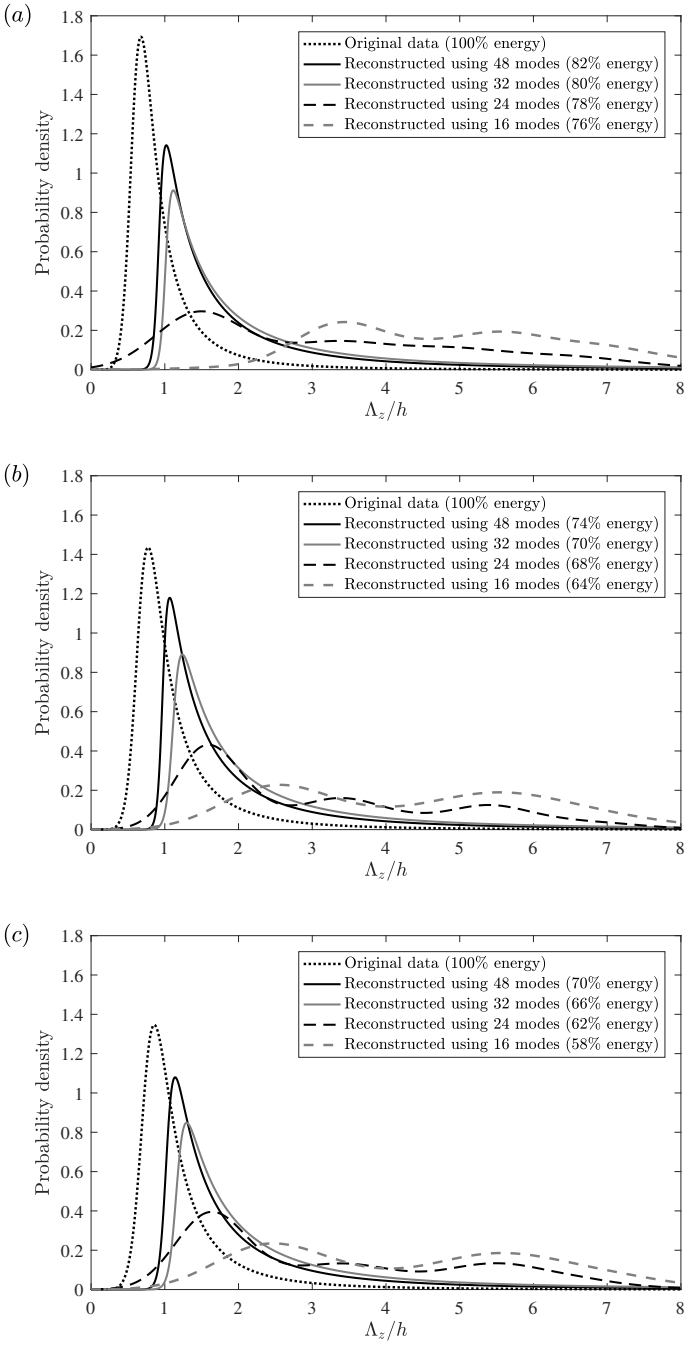

FIGURE 14. Effect of number of modes used in POD reconstruction on the probability density functions of the distances between low-speed zones (Λ_z) in the wake at $x = 2h$ for (*a*) $Re(h) = 3500$, (*b*) $Re(h) = 5200$, and (*c*) $Re(h) = 7000$. The distributions were calculated using the same spatial autocorrelation that is covered in section 3.4. The distributions are highly sensitive to the number of POD modes used in reconstruction of the data.

	$Re(h)$ range	Aspect ratio(s)	Dominant mode(s)	Wavelength(s)
Present investigation	3500-7000	46.5	B	0.7-0.8h
Naghib-Lahouti *et al.* (2014)	2000-50000	12.5	B′	2.3-2.5h
Naghib-Lahouti *et al.* (2012)	250-2150	12.5	B′	2.0-2.5h
Ryan *et al.* (2005)	Up to 700	2.5-17.5	B′, S′	2.2h, 0.7-1.0h

TABLE 3. Summary of the present and past investigations.

did not change greatly as the upstream boundary layer transitioned from laminar to turbulent. Only a slight increase in the secondary instability wavelength was observed, along with an expected increase in wake turbulence.

The characteristics of the secondary instability described above match those of the cylinder mode B and all features agree with the mode B models that have been proposed by Brede *et al.* (1996) and Williamson (1996*a*) for the wakes of circular cylinders. The present results do not suggest extrapolation of the stability analysis of Ryan *et al.* (2005) to higher Re and AR as is evident in the summary given by table 3. Their analysis predicted that elongated blunt body wakes with $AR > 7.5$ would be afflicted by modes that differ from those of circular cylinders at Re smaller than 700. No evidence of their predicted modes B′ nor S′ has been found in the present study, although it should be emphasised that the present investigation was performed on an elongated blunt body with larger Re and AR than what Ryan *et al.* (2005) considered in their stability analysis.

The present investigation also shows different results compared with the works of Naghib-Lahouti *et al.* (2012, 2014). They concluded the presence of mode B′ with secondary instability wavelengths ranging from 2.0 to 2.5h in the wake of an elongated blunt body with a much smaller AR of 12.5 for $250 \leqslant Re(h) \leqslant 5 \times 10^4$ as shown by table 3. The same indirect POD-based characterisation of the secondary instability used in these studies was repeated here. It was shown that the use of POD for characterising the secondary instability in the wake is highly sensitive to the amount of energy captured (number of modes used) by the data reconstruction. This may also explain the large differences between the model proposed by Naghib-Lahouti *et al.* (2012) and the models of Brede *et al.* (1996) and Williamson (1996*a*), as the former was influenced by the indirect POD-based analysis. Further investigation of the secondary instability by direct characterisation of the vortical structures in the wake of elongated bodies with small AR is suggested.

Finally, the present investigation showed that the average strength of the streamwise vortices in the upstream boundary layer was nearly an order of magnitude less than the average strength of the streamwise vortices in the wake. It was also shown that the boundary layer streaks are quickly replaced by the wake structures over the region $0 < x < h$. These observations, when coupled with the fact that the state of the upstream boundary layer does not significantly affect the secondary instability in the wake, suggest that the upstream boundary layer structures are simply absorbed into the near-wake region without having much of an impact on the wake organisation. This also implies that the state of the upstream boundary layer does not play much of a role in the development of the secondary instability. This result is congruent with the findings of Naghib-Lahouti *et al.* (2014), who concluded that the secondary instability has little dependence on the state of the upstream boundary layer.

Acknowledgements

This work has been supported by the Natural Sciences and Engineering Research Council of Canada (grant number 2016-04646). The authors would like to thank Dr. David Nobes for allowing us to use his Imager ProX-4M cameras during our experiments, and Bernie Faulkner for manufacturing the elongated blunt body model.

REFERENCES

Badri Narayanan, M. A. & Ramjee, V. 1969 On the criteria for reverse transition in a two-dimensional boundary layer flow. *J. Fluid Mech.* **35** (2), 225–241.

Baker, J. P., Mayda, E. A. & van Dam, C. P. 2006 Experimental analysis of thick blunt trailing-edge wind turbine airfoils. *J. Sol. Energy Eng.* **128** (4), 422–431.

Bays-Muchmore, B. & Ahmed, A. 1993 On streamwise vortices in turbulent wakes of cylinders. *Phys. Fluids A* **5** (2), 387–392.

Berkooz, G., Holmes, P. & Lumley, L. 1993 The proper orthogonal decomposition in the analysis of turbulent flows. *Annu. Rev. Fluid Mech.* **25**, 539–575.

Blackburn, H. M. & Lopez, J. M. 2003 On three-dimensional quasiperiodic Floquet instabilities of two-dimensional bluff body wakes. *Phys. Fluids* **15** (8), L57.

Blackburn, H. M., Marques, F. & Lopez, J. M. 2005 Symmetry breaking of two-dimensional time-periodic wakes. *J. Fluid Mech.* **522**, 395–411.

Blackwelder, R. F. & Eckelmann, H. 1979 Streamwise vortices associated with the bursting phenomenon. *J. Fluid Mech.* **94** (3), 577–594.

Blackwelder, R. F. & Kovasznay, L. S. G. 1972 Large-scale motion of a turbulent boundary layer during relaminarization. *J. Fluid Mech.* **53** (1), 61–83.

Bloor, M. S. 1964 The transition to turbulence in the wake of a circular cylinder. *J. Fluid Mech.* **19** (2), 290–304.

Brede, M., Eckelmann, H. & Rockwell, D. 1996 On secondary vortices in the cylinder wake. *Phys. Fluids* **8** (8), 2117–2124.

Brooks, T. F., Pope, D. S. & Marcolini, M. A. 1989 Airfoil self-noise and prediction. *NASA Ref. Publ. 1218* .

Gerrard, J. H. 1966 The mechanics of the formation region of vortices behind bluff bodies. *J. Fluid Mech.* **25** (2), 401–413.

Gerrard, J. H. 1978 The wakes of cylindrical bluff bodies at low Reynolds number. *Phil. Trans. R. Soc. A* **288** (1354), 351–382.

Ghaemi, S., Ragni, D. & Scarano, F. 2012 PIV-based pressure fluctuations in the turbulent boundary layer. *Exp. Fluids* **53** (6), 1823–1840.

Jackson, K. J., Zuteck, M. D., van Dam, C. P., Standish, K. J. & Berry, D. 2005 Innovative design approaches for large wind turbine blades. *Wind Energ.* **8** (2), 141–171.

Jeong, J. & Hussain, F. 1995 On the identification of a vortex. *J. Fluid Mech.* **285**, 69–94.

Johnson, M. R. & Kostiuk, L. W. 2000 Efficiencies of low-momentum jet diffusion flames in crosswinds. *Combust. Flame* **123** (1), 189–200.

Lin, J., Laval, J. P., Foucaut, J. M. & Stanislas, M. 2008 Quantitative characterization of coherent structures in the buffer layer of near-wall turbulence. Part 1: streaks. *Exp. Fluids* **45** (6), 999–1013.

Lin, J. C., Towfighi, J. & Rockwell, D. 1995 Instantaneous structure of the near-wake of a circular cylinder: On the effect of Reynolds number. *J. Fluids Struct.* **9** (4), 409–418.

Luo, S. C., Tong, X. H. & Khoo, B. C. 2007 Transition phenomena in the wake of a square cylinder. *J. Fluids Struct.* **23** (2), 227–248.

Mansy, H., Yang, P. M. & Williams, D. R. 1994 Quantitative measurements of three-dimensional structures in the wake of a circular cylinder. *J. Fluid Mech.* **270**, 277–296.

Meinhart, C. D., Wereley, S. T. & Santiago, J. G. 2000 A PIV algorithm for estimating time-averaged velocity fields. *J. Fluids Eng.* **122** (2), 285–289.

Naghib-Lahouti, A., Doddipatla, L. S. & Hangan, H. 2012 Secondary wake instabilities of a blunt trailing edge profiled body as a basis for flow control. *Exp. Fluids* **52** (6), 1547–1566.

Naghib-Lahouti, A., Lavoie, P. & Hangan, H. 2014 Wake instabilities of a blunt trailing edge profiled body at intermediate Reynolds numbers. *Exp. Fluids* **55** (7), 1779.

Patel, V. C. & Head, M. R. 1968 Reversion of turbulent to laminar flow. *J. Fluid Mech.* **34** (2), 371–392.

Petrusma, M. S. & Gai, S. L. 1996 Bluff body wakes with free, fixed, and discontinuous separation at low Reynolds numbers and low aspect ratio. *Exp. Fluids* **20** (3), 189–198.

Robichaux, J., Balachandar, S. & Vanka, S. P. 1999 Three-dimensional Floquet instability of the wake of square cylinder. *Phys. Fluids* **11** (3), 560–578.

Roshko, A. 1954 On the development of turbulent wakes from vortex streets. *NACA rep. 1191* .

Roshko, A. 1993 Perspectives on bluff body aerodynamics. *J. Wind Eng. Ind. Aerodyn.* **49** (1), 79–100.

Ryan, K., Thompson, M. C. & Hourigan, K. 2005 Three-dimensional transition in the wake of bluff elongated cylinders. *J. Fluid Mech.* **538**, 1–29.

Scarano, F. & Poelma, C. 2009 Three-dimensional vorticity patterns of cylinder wakes. *Exp. Fluids* **47** (1), 69–83.

Schoppa, W. & Hussain, F. 2002 Coherent structure generation in near-wall turbulence. *J. Fluid Mech.* **453**, 57–108.

Sheard, G. J., Fitzgerald, M. J. & Ryan, K. 2009 Cylinders with square cross-section: wake instabilities with incidence angle variation. *J. Fluid Mech.* **630**, 43–69.

Sheather, S. J. 2004 Density estimation. *Stat. Sci.* **19** (4), 588–597.

Sirovich, L. 1987 Turbulence and the dynamics of coherent structures, parts I-III. *Q. Appl. Math.* **45**, 561–590.

Smith, C. R. & Metzler, S. P. 1983 The characteristics of low-speed streaks in the near-wall region of a turbulent boundary layer. *J. Fluid Mech.* **129**, 27–54.

Standish, K. J. & van Dam, C. P. 2003 Aerodynamic analysis of blunt trailing edge airfoils. *J. Sol. Energy Eng.* **125** (4), 479–487.

Tadikamalla, P. R. 1980 A look at the Burr and related distributions. *Int. Stat. Rev.* **48** (3), 337–344.

Thompson, M. C., Leweke, T. & Williamson, C. H. K. 2001 The physical mechanism of transition in bluff body wakes. *J. Fluids Struct.* **15** (3), 607–616.

Tomkins, C. D. & Adrian, R. J. 2003 Spanwise structure and scale growth in turbulent boundary layers. *J. Fluid Mech.* **490**, 37–74.

Wei, T. & Smith, C. R. 1986 Secondary vortices in the wake of circular cylinders. *J. Fluid Mech.* **169**, 513–533.

Westerweel, J. & Scarano, F. 2005 Universal outlier detection for PIV data. *Exp. Fluids* **39** (6), 1096–1100.

Wieneke, B. 2005 Stereo-PIV using self-calibration on particle images. *Exp. Fluids* **39** (2), 267–280.

Williamson, C. H. K. 1988 The existence of two stages in the transition to three-dimensionality of a cylinder wake. *Phys. Fluids* **31** (11), 3165–3168.

Williamson, C. H. K. 1989 Oblique and parallel modes of vortex shedding in the wake of a circular cylinder at low Reynolds numbers. *J. Fluid Mech.* **206**, 579–627.

Williamson, C. H. K. 1992 The natural and forced formation of spot-like 'vortex dislocations' in the transition of a wake. *J. Fluid Mech.* **243**, 393–441.

Williamson, C. H. K. 1996*a* Three-dimensional wake transition. *J. Fluid Mech.* **328**, 345–407.

Williamson, C. H. K. 1996*b* Vortex dynamics in the cylinder wake. *Annu. Rev. Fluid Mech.* **28**, 477–539.

Williamson, C. H. K. & Govardhan, R. 2004 Vortex-induced vibrations. *Annu. Rev. Fluid Mech.* **36**, 413–455.

Wu, J., Sheridan, J., Soria, J. & Welsh, M. C. 1994 An experimental investigation of streamwise vortices in the wake of a bluff body. *J. Fluids Struct.* **8** (6), 621–625.

Wu, J., Sheridan, J., Welsh, M. C. & Hourigan, K. 1996 Three-dimensional vortex structures in a cylinder wake. *J. Fluid Mech.* **312**, 201–222.

Yildirim, I., Rindt, C. C. M. & van Steenhoven, A. A. 2013 Mode C flow transition behind a circular cylinder with a near-wake wire disturbance. *J. Fluid Mech.* **727**, 30–55.

Zdravkovich, M. M. 1969 Smoke observations of the formation of a kármán vortex street. *J. Fluid Mech.* **37** (3), 491–496.

Zhang, H. Q., Fey, U., Noack, B. R., König, M. & Eckelmann, H. 1995 On the transition of the cylinder wake. *Phys. Fluids* **7** (4), 779–794.